

Numerical simulation of flow past a rotating and rotary oscillating circular cylinder on unstructured meshes

Wei Bai*

Department of Civil and Environmental Engineering, National University of Singapore, 1 Engineering Drive 2, Singapore 117576, Singapore

(Received March 8, 2013, Revised June 6, 2013, Accepted July 25, 2013)

Abstract. The unsteady flow past a circular cylinder which starts rotating or rotary oscillating impulsively from rest in a viscous fluid is investigated for Reynolds numbers $Re = 200$ and 1000 , rectilinear speed ratios α between 0.5 and 5.0 , and forced oscillating frequencies f_s between 0.1 and 2.0 . Numerical solutions of the Navier-Stokes equations are obtained by using a finite volume method on an unstructured collocated grid. The objective of the study is to examine the effect of the rotating and rotary oscillating circular cylinder on the flow patterns and dynamics loads. The numerical results reveal that the Kármán vortex street vanishes entirely behind the rotating cylinder when the ratio α exceeds the critical value, and the vortex shedding behind the rotary oscillating cylinder undergoes mainly three modes named ‘synchronization’, ‘competition’ and ‘natural shedding’ with the increase of f_s . Based on the amplitude spectra analysis of the lift coefficients, the regions of the classification of flow structure modes are presented, which provide important references for the flow control in the ocean engineering.

Keywords: rotating cylinder; rotary oscillating cylinder; navier-stokes equations; unstructured meshes; vortex shedding patterns

1. Introduction

The viscous flow interaction with a moving circular cylinder exists widely in the ocean engineering, aircraft and heat energy engineering, which has applications in active or feedback control of vortex shedding, with consequences for the wake modification and the reduction of flow induced vibrations (Mittal 2001). It is also of importance in the investigation of the unsteady flow separation and the boundary layer control. Therefore, the study of the wake behind the moving circular cylinder and the dynamic features of the flow field has attracted a great deal of attention.

For the flow associated with a circular cylinder of radius a , which starts its motion impulsively from rest with a uniform rectilinear velocity U_∞ and an invariant angular velocity Ω in the counterclockwise direction, the flow field depends mainly on two parameters. The first is the Reynolds number

* Corresponding author, Assistant Professor, E-mail: w.bai@nus.edu.sg

$$\text{Re} = \frac{2U_{\infty}a}{\nu} \quad (1)$$

where ν is the kinematic viscosity of the fluid. The second is the rectilinear speed ratio

$$\alpha = \frac{\Omega a}{U_{\infty}} \quad (2)$$

In the aspect of experimental studies on this problem, Prandtl (1925) carried out the earliest visual experiments of flow past a rotating cylinder. After that, Swanson (1961) measured the lift and drag forces directly. In the early 1980s several experimental studies were reported, for example Taneda (1980), Koromilas and Telionis (1980), and Diaz *et al.* (1983). Among those works, Matsui (1982) found that when the ratio α is moderately high, a Kármán vortex street, Görtler-type vortices and Taylor vortices are generated at the same time. In particular, Coutanceau and Menard (1985) investigated the early phase of the establishment of the flow for $\text{Re} = 200$, $0.5 \leq \alpha \leq 3.25$ by visualizing the flow patterns with solid tracers, and reported that Kármán vortex street disappeared entirely during the early stage of their experiment when the ratio α is greater than a certain limiting value. In addition, the experimental flow visualization was also conducted by Badr *et al.* (1990) for $\text{Re} = 1000$ and $0.5 \leq \alpha \leq 3.0$, Lam (2009) for $3600 \leq \text{Re} \leq 5000$ and $\alpha \leq 2.5$.

The solutions of the Navier-Stokes equations using computational methods provide an excellent alternative description of the viscous fluid motions. Badr and Dennis (1985) and Badr *et al.* (1990) investigated the flow past a circular cylinder which begins translational and rotational motion impulsively from rest using the Fourier analysis, and compared the numerical and experimental results for $200 \leq \text{Re} \leq 10^4$ and $0.5 \leq \alpha \leq 3.0$. For $10^3 \leq \text{Re} \leq 10^6$ and $0 \leq \alpha \leq 2.0$, the initial stage of the flow has been studied by Cheng and Chern (1991) using a hybrid vortex method. In addition, Chen *et al.* (1993) computed numerically a velocity-vorticity formulation of the Navier-Stokes equations for $\text{Re} = 200$ and $0.5 \leq \alpha \leq 3.25$, and Chew *et al.* (1995) obtained the flow structure, the force coefficients and the Strouhal number for $\text{Re} = 1000$ and $0 \leq \alpha \leq 6$ by a hybrid vortex scheme. The more recent numerical works include the study of a rotating cylinder with cross flow oscillation by Nobari and Ghazanfarian (2009), two rotating side-by-side circular cylinders by Yoon *et al.* (2009), rotating cylinders next to a wall by Rao *et al.* (2011), and a rotating cylinder in turbulent flows by Karabelas (2010).

For the uniform flow of velocity U_{∞} associated with a circular cylinder of radius a which starts its forced oscillating motion impulsively from rest with a sinusoidal variant angular velocity, the flow structure depends mainly on three parameters. The first two are the Reynolds number Re and the rectilinear speed ratio α as discussed before, and the third one is the forced oscillating frequency

$$f_s = \frac{\tilde{f}_s a}{U_{\infty}} \quad (3)$$

where \tilde{f}_s is the dimensional forced oscillating frequency. In this case, the forced oscillating frequency and the natural shedding frequency have great influences upon the flow development all together. The competitive relationship between these two frequencies results in the complex

unsteady features of the wake flow, which are still not fully understood.

Most of the prior studies on the effect of cylinder oscillation were made experimentally. Okajima *et al.* (1975) examined the forces acting on a rotary oscillating cylinder for $40 \leq Re \leq 6000$, $0.2 \leq \alpha \leq 1.0$, and $0.025 \leq f_s \leq 0.15$. When the oscillating frequency is close to the natural vortex shedding frequency, he noted a ‘synchronization’ similar to that observed, for example, by Bishop and Hassan (1964) and Koopman (1967). Tokumaru and Dimotakis (1991) investigated the effect of the rotary oscillating cylinder on the wake structure for $Re = 1.5 \times 10^4$ by visualizing the flow patterns, and reported that vortex shedding behind the cylinder undergoes mainly three modes, named ‘synchronization’, ‘competition’, and ‘natural shedding’. At lower oscillating frequency, the wake structure is synchronized by the forced cylinder oscillation. With increasing the forced frequency, the wake pattern turns to be transitional mode due to the competition between the forced oscillating frequency and the natural shedding frequency. At higher oscillating frequency the vortex shedding pattern is similar to that of flow past a stationary circular cylinder, and alternate shedding vortex forms Kármán vortex street. Moreover, the transition between ‘synchronization’ and ‘natural shedding’ modes occurs gradually through ‘competition’ mode.

However, a relatively smaller number of researchers have simulated numerically the effects of rotary oscillation of the cylinder. Lu and Zhuang (1994) investigated the flow structures of viscous flow past a rotary oscillating circular cylinder in a uniform stream at $Re = 1000$. They adopted the finite difference method to calculate a stream-vorticity formulation of the Navier-Stokes equations in frame of the polar coordinate system. They also presented a parameter map in the frequency-amplitude plane for indicating the classification of vortex structures in the near wake. Moreover, Baek and Sung (1998) utilized a fractional-step method to solve the Navier-Stokes equations with a generalized coordinate system.

In this paper, the numerical calculation is performed to simulate the flow past a rotating and rotary oscillating circular cylinder. Unlike the numerical methods used before, a finite volume method based on unstructured colocated meshes is adopted here to solve the Navier-Stokes equations with original variables. Most previous methods for this problem are constructed in frame of the nonorthogonal coordinate system, and the viscous vorticity function is introduced as the unknown variable. They are not robust enough to be suitable for arbitrary computational boundaries, and it is also difficult to define the boundary conditions exactly. However, the unstructured grids in the Cartesian coordinate system used here are efficient for arbitrary complex domains, and they are clear and straightforward from the physical point of view. Numerical results include the vortex shedding and the full development of the wake behind the rotating and rotary oscillating cylinder. The main effort of this paper is devoted to analysis the global characteristics of the flow, such as the lift and drag coefficients at different values of the rotational parameters and the amplitude spectra analysis of the lift coefficients based on which the regions of the classification of flow patterns are provided for both the rotating and rotary oscillating cylinders.

2. Governing equations and boundary conditions

To describe an unsteady, incompressible two-dimensional viscous flow, a right-handed Cartesian coordinate system Oxy is defined as shown in Fig. 1. Based on the dimensionless variables defined according to

$$\mathbf{x} = \frac{\tilde{\mathbf{x}}}{a}, \quad u = \frac{\tilde{u}}{U_\infty}, \quad v = \frac{\tilde{v}}{U_\infty}, \quad p = \frac{\tilde{p}}{\rho U_\infty^2}, \quad t = \frac{\tilde{t}}{a/U_\infty} \quad (4)$$

the continuity and Navier-Stokes equations can be expressed in dimensionless form as

$$\frac{\partial u}{\partial x} + \frac{\partial v}{\partial y} = 0 \quad (5)$$

$$\frac{\partial u}{\partial t} + u \frac{\partial u}{\partial x} + v \frac{\partial u}{\partial y} = -\frac{\partial p}{\partial x} + \frac{2}{\text{Re}} \left(\frac{\partial^2 u}{\partial x^2} + \frac{\partial^2 u}{\partial y^2} \right) \quad (6)$$

$$\frac{\partial v}{\partial t} + u \frac{\partial v}{\partial x} + v \frac{\partial v}{\partial y} = -\frac{\partial p}{\partial y} + \frac{2}{\text{Re}} \left(\frac{\partial^2 v}{\partial x^2} + \frac{\partial^2 v}{\partial y^2} \right) \quad (7)$$

where the tilde denotes the dimensional variables. $\mathbf{x} = (x, y)$ is the position vector, $\mathbf{u} = (u, v)$ are the velocity components in the Cartesian directions x and y respectively, ρ is the fluid density, p denotes the pressure and t is the time.

In addition the boundary conditions must be satisfied on the boundary surfaces of the computational domain. On the inlet boundary, the fluid velocity equals to the prescribed inlet velocity \mathbf{u}_{in} . The slip boundary condition is applied on two sidewalls, in order to eliminate the boundary influence on the numerical results. In the computations generally a very wide computational domain is chosen so that the effect of the sidewalls is negligible. However, the non-slip condition must be specified on the cylinder surface. On a rotating circular cylinder the boundary condition can be given as

$$u = -\alpha y, \quad v = \alpha x \quad (8)$$

while the boundary condition on a rotary oscillating circular cylinder becomes

$$u = -\alpha y \sin(2\pi f_s t), \quad v = \alpha x \sin(2\pi f_s t) \quad (9)$$

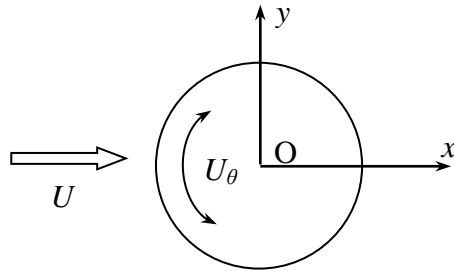


Fig. 1 The sketch of definition

On the outlet boundary the condition should make the boundary “transparent”, i.e., the numerical solutions in the computational domain would not be affected by the outlet boundary, wherever it is placed. The outlet boundary condition will be discussed in detail later.

3. Discretization of momentum equations

The present numerical method is developed on an unstructured triangular grid. It is known that the unstructured grid is very suitable for complicated computational domains and the Delaunay triangulation technique is a popular method to generate the triangular grid, which is adopted here. In the Delaunay triangulation method the first step is to generate the initial triangles, based on the given points on the known computational boundaries. Once the coarse Delaunay initial triangles are generated a certain amount of points can be inserted in the domain to form the final grid. The number of the inserted points is defined by users, but the position of the inserted points is determined by the Delaunay triangulation method. In addition, if local refinement is demanded some representative points on the boundary of the refined region can be specified in accompany with the boundary points. These representative points are used as part of the prescribed boundary points in the generation of the initial triangles, as shown in the regions around the cylinder as well as behind it in Fig. 2(a). Fig. 2(b) shows the results of the Delaunay triangulation method generated for the exterior flow around a circular cylinder. It should be noted that for moving bodies, the boundary points will be updated every time step, therefore, the abovementioned mesh generation procedure can be implemented every time step in order to accommodate the change of the computational domain.

On the unstructured triangular grid, the cell-centered Finite Volume Method (FVM) is used here to obtain the Navier-Stokes solutions. For each triangular Control Volume (CV) P_0 , the momentum equation in integral form is

$$V_{P_0} \left(\frac{\partial \phi}{\partial t} \right)_{P_0} + \sum_{j=1}^3 \int_{S_j} \left(\mathbf{u} \phi - \frac{2}{\text{Re}} \nabla \phi \right) \cdot d\mathbf{S} = -V_{P_0} \nabla p_{P_0} \quad (10)$$

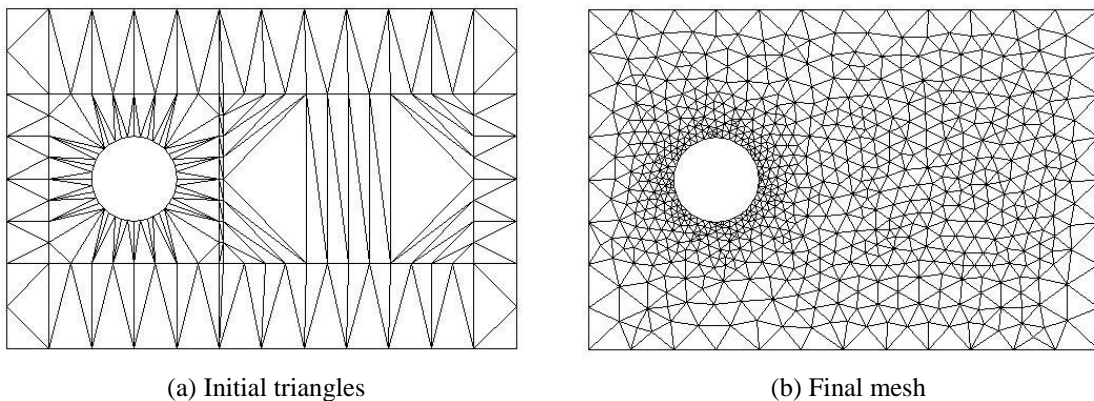


Fig. 2 An example mesh generated for a flow past a circular cylinder for illustration of the mesh generation

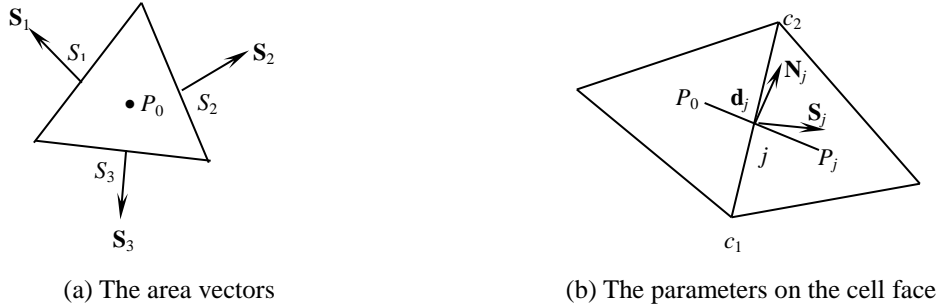


Fig. 3 Definition of geometrical parameters in a control volume

where ϕ is the general variable denoting u or v in the corresponding directions respectively, V_{P_0} is the volume of CV P_0 , \mathbf{S} is the area vector pointing out of CV P_0 (see Fig. 3(a)). The discretization of each term in Eq. (10) is discussed in the following.

3.1 The convective fluxes

The convective fluxes on the j th face of CV P_0 is defined by C_j ,

$$C_j = \int_{S_j} \mathbf{u} \phi \cdot d\mathbf{S} \approx (\mathbf{u} \phi)_j \cdot \mathbf{S}_j = (\mathbf{u}_j \cdot \mathbf{S}_j) \phi_j = F_j \phi_j \quad (11)$$

where F_j is the mass fluxes on the j th cell face, and the cell face velocity \mathbf{u}_j can be determined by the momentum interpolation method,

$$\mathbf{u}_j = \frac{1}{2}(\mathbf{u}_{P_0} + \mathbf{u}_{P_j}) - \frac{1}{2} \left[\left(\frac{V}{a_0} \right)_{P_0} + \left(\frac{V}{a_0} \right)_{P_j} \right] \left[\frac{p_{P_j} - p_{P_0}}{|\mathbf{d}_j|} - \frac{1}{2}(\nabla p_{P_0} + \nabla p_{P_j}) \cdot \frac{\mathbf{d}_j}{|\mathbf{d}_j|} \right] \frac{\mathbf{S}_j}{|\mathbf{S}_j|} \quad (12)$$

where P_j is the j th CV adjacent to the CV P_0 , a_0 denotes the diagonal coefficient in the discretized momentum equation discussed below in Eq. (22), and \mathbf{d}_j is the distance vector between the nodes P_0 and P_j (see Fig. 3(b)). The above equation shows that the cell face velocity consists of three terms. The first term is the linear interpolation of the velocity, the second term is the pressure gradient under the linear assumption of the pressure and the third term is the averaged pressure gradient over the two adjacent cells. This momentum interpolation equation is used only in discretizing the momentum equations, while the linear interpolation is adopted to discretize the continuity equation. The practice indicates that the unphysical pressure field can be avoided if this pressure-velocity coupling is introduced in any step of the computational procedure.

Different approximations of the cell face variables ϕ_j will introduce different convective schemes. By using the simplest first-order upwind difference scheme (UDS), Eq. (11) can be expressed as

$$C_j = \max[F_j, 0] \phi_{P_0} + \min[F_j, 0] \phi_{P_j} \quad (13)$$

However, it is well known that the serious numerical diffusion appears when *UDS* is adopted. Therefore, the second-order upwind difference scheme (*SUDS*) is implemented here to discretize the convective fluxes,

$$\phi_j = \begin{cases} \phi_{P_0} + (\nabla \phi)_{P_0} \cdot \Delta \mathbf{r}_{j,P_0} & F_j \geq 0 \\ \phi_{P_j} + (\nabla \phi)_{P_j} \cdot \Delta \mathbf{r}_{j,P_j} & F_j < 0 \end{cases} \quad (14)$$

where $\Delta \mathbf{r}_{j,P_0}$ and $\Delta \mathbf{r}_{j,P_j}$ are the distance vector between the midpoint j on the cell face and the nodes P_0, P_j respectively. After modified by the deferred correction method, Eq. (11) can then be written as

$$C_j = F_j \phi_j^{UDS} + F_j \left(\phi_j^{SUDS} - \phi_j^{UDS} \right)^{n-1} \quad (15)$$

where the superscripts *UDS* and *SUDS* stand for the variables approximated by the first-order and second-order upwind difference schemes respectively, and the superscript $n-1$ denotes that the terms in the bracket are calculated using the values obtained from the previous iteration. The second-order approximation in the bracket is added to the source term, and the first-order scheme is adopted to compute the coefficient matrix. When the calculation is convergent, the contribution of the first-order scheme will vanish and the second-order accuracy can be achieved.

3.2 The diffusive fluxes

By assuming that the diffusive fluxes on the j th cell face of CV P_0 is D_j , we have

$$D_j = - \int_{s_j} \frac{2}{\text{Re}} \nabla \phi \cdot d\mathbf{S} \approx - \frac{2}{\text{Re}} \nabla \phi_j \cdot \mathbf{S}_j \quad (16)$$

D_j can be further decomposed into the normal diffusion D_j^n and the cross diffusion D_j^c ,

$$D_j = D_j^n + D_j^c = - \frac{2}{\text{Re}} \left(\frac{\phi_{P_j} - \phi_{P_0}}{|\mathbf{d}_j|} \frac{\mathbf{d}_j}{|\mathbf{d}_j|} \right) \cdot \mathbf{S}_j - \frac{2}{\text{Re}} \left(\frac{\phi_{c_2} - \phi_{c_1}}{l_{c_1,c_2}} \frac{\mathbf{N}_j}{|\mathbf{N}_j|} \right) \cdot \mathbf{S}_j \quad (17)$$

where \mathbf{N}_j is the conjugation of \mathbf{d}_j , l_{c_1,c_2} is the distance between the vertexes c_1 and c_2 on the j th cell face of CV P_0 , as shown in Fig. 3(b). ϕ_{c_1}, ϕ_{c_2} are the ϕ values on c_1, c_2 obtained by the following interpolation,

$$\phi_c = \frac{\sum_{i=1}^N \omega_i \phi_i}{\sum_{i=1}^N \omega_i} \quad (18)$$

where N is the number of neighboring triangles around the vertex, and ω_i is the weight factor taken as the reciprocal of the distance between the vertex and the neighboring cell center.

It should be mentioned that the triangles generated by the Delaunay triangulation method are almost regular, $\mathbf{N}_j \cdot \mathbf{S}_j$ is thus close to zero, and D_j^c is usually much smaller than D_j^n . In discretizing the equations, D_j^n is treated implicitly as the unknown and D_j^c is considered explicitly.

3.3 The other terms

The evaluation of the pressure gradient is needed in Eqs. (10), (12) and (14). Using the Gauss' Theorem, we can obtain the following formulation to calculate the pressure gradient,

$$V_{P_0} \nabla p_{P_0} = \sum_{j=1}^3 p_j \mathbf{S}_j \quad (19)$$

where p_j is the pressure on the j th cell face of CV P_0 , predicted by the linear interpolation of the pressure in two adjacent cells.

An implicit three-level scheme of second-order accuracy is adopted here to approximate the unsteady term in Eq. (10),

$$\frac{\partial \phi}{\partial t} = \frac{3\phi^n - 4\phi^{n-1} + \phi^{n-2}}{2\Delta t} \quad (20)$$

where Δt is the time interval, the superscripts n , $n-1$, and $n-2$ denote the values at three time levels, t_n , t_{n-1} , and t_{n-2} respectively. At the first time step, only the results at the previous time level are known, so the first-order implicit Euler scheme is introduced. Therefore, the universal equation for the discretization of the unsteady term is

$$\frac{\partial \phi}{\partial t} = \frac{(1+0.5\lambda)\phi^n - (1+\lambda)\phi^{n-1} + 0.5\lambda\phi^{n-2}}{\Delta t} \quad (21)$$

where $\lambda = 1$ corresponds to the implicit three-level scheme, and $\lambda = 0$ indicates the implicit Euler scheme.

3.4 Establishment of the discretized momentum equations

Substituting all the discretization schemes into Eq. (10) results in the final discretized momentum equation of CV P_0 ,

$$a_0 \phi_{P_0} = \sum_{j=1}^3 a_j \phi_{P_j} + b_0 \quad (22)$$

where

$$a_j = -\min[F_j, 0] + \frac{2}{\text{Re}} \frac{\mathbf{d}_j \cdot \mathbf{S}_j}{|\mathbf{d}_j|^2} \quad (23)$$

$$a_0 = \sum_{j=1}^3 a_j + \frac{\rho V_{P_0}}{\Delta t} (1+0.5\lambda) \quad (24)$$

$$b_0 = \sum_{j=1}^3 \left[-p_j \mathbf{S}_j - F_j (\phi_j^{SUDS} - \phi_j^{UDS})^{n-1} + \frac{2}{\text{Re}} \left(\frac{\phi_{c_2} - \phi_{c_1} \mathbf{N}_j}{l_{c_1, c_2} |\mathbf{N}_j|} \right) \cdot \mathbf{S}_j \right] + \frac{\rho V_{P_0}}{\Delta t} [(1 + \lambda) \phi_{P_0}^{n-1} - 0.5 \lambda \phi_{P_0}^{n-2}] \quad (25)$$

The under-relaxation technique is always used in the numerical computation in order to ensure the convergence of the iterative procedure. For the momentum equations the under-relaxation factor is considered directly in assembling the coefficient matrix, and the complete algebraic equation adopted in the present numerical simulation is

$$\begin{pmatrix} a_0 \\ \alpha_\phi \end{pmatrix} \phi_{P_0} = \sum_{j=1}^3 a_j \phi_{P_j} + b_0 + (1 - \alpha_\phi) \frac{a_0}{\alpha_\phi} \phi_{P_0}^{n-1} \quad (26)$$

where α_ϕ is the under-relaxation factor for the variable ϕ , which is taken as 0.7 in this study.

4. The pressure correction equation

The velocity obtained from the solution of the momentum equations cannot be guaranteed to satisfy the continuity equation, which needs to be corrected subsequently by an appropriate algorithm. Here the SIMPLE algorithm is adopted, in which the cell face velocity correction \mathbf{u}'_j is defined in terms of the pressure correction p' ; more details about the SIMPLE algorithm can be found in many textbooks, such as Ferziger and Perić (1999).

$$\mathbf{u}'_j = -\frac{1}{2} \left[\left(\frac{V}{a_0^u} \right)_{P_0} + \left(\frac{V}{a_0^u} \right)_{P_j} \right] \left[\left(\frac{p'_{P_j} - p'_{P_0}}{|\mathbf{d}_j|} \right) \frac{\mathbf{S}_j}{|\mathbf{S}_j|} \right] \quad (27)$$

where p'_{P_0} and p'_{P_j} are the pressure corrections in CV P_0 and CV P_j respectively, and a_0^u is the diagonal coefficient in the discretized momentum equations.

Substituting Eq. (27) into the continuity equation leads to the discretized pressure correction equation for p'_{P_0} ,

$$a_0^p p'_{P_0} = \sum_{j=1}^3 a_j^p p'_{P_j} + b_0^p \quad (28)$$

where the superscript p denotes that the corresponding coefficients are of the pressure correction equation. The coefficients are given by

$$a_j^p = \frac{1}{2} \left[\left(\frac{V}{a_0^u} \right)_{P_0} + \left(\frac{V}{a_0^u} \right)_{P_j} \right] \left| \frac{\mathbf{S}_j}{\mathbf{d}_j} \right| \quad (29)$$

$$a_0^p = \sum_{j=1}^3 a_j^p \quad (30)$$

$$b_0^p = -\sum_{j=1}^3 F_j \quad (31)$$

After obtaining the pressure correction p'_{P_0} , the pressure and the velocity can be corrected by

$$P_{P_0} = P_{P_0}^* + p'_{P_0} \quad (32)$$

$$\mathbf{u}_{P_0} = \mathbf{u}_{P_0}^* - \frac{V_{P_0}}{a_0^u} \nabla p'_{P_0} = \mathbf{u}_{P_0}^* - \sum_{j=1}^3 \frac{p'_j \mathbf{S}_j}{a_0^u} \quad (33)$$

5. The outlet boundary condition

The implementation of an appropriate outlet boundary condition is an important issue in CFD, which could affect directly the accuracy and the simulating time in a reasonably sized domain. There are many types of the outlet boundary conditions, each of which has its own feature and advantage. The outlet boundary condition applied in this paper is that the normal velocity satisfies the local mass conservation and the tangent velocity is subject to the Neumann condition (Li and Tao 1993). In order to illustrate conveniently, we only consider the outlet boundary surface perpendicular to the x -axis, where the normal and tangent velocities are the components u and v respectively.

Firstly, the v component satisfied the Neumann condition is written easily as

$$v_j = v_{P_0}^{n-1} \quad (34)$$

where v_j is the v component of the boundary node j , v_{P_0} is the v component of CV P_0 adjacent to the boundary node j . The application of the local mass conservation in CV P_0 yields

$$\sum_{i=1}^3 \mathbf{u}_i \cdot \mathbf{S}_i = 0 \quad (35)$$

Consequently, we can find the normal velocity of the boundary node j ,

$$u_j = \frac{1}{S_{jx}} \left(-\sum_{i=1}^2 \mathbf{u}_i \cdot \mathbf{S}_i - v_j S_{jy} \right) \quad (36)$$

where $(S_{jx}, S_{jy}) = \mathbf{S}_j$ are the area vector components in the x and y directions respectively. As the distribution of the normal velocity still needs to satisfy the global mass conversation, a constant C is introduced to correct the normal velocity u_j , which is defined by

$$\sum_{j=1}^M (u_j + C) S_{jx} = Flow_{in} \tag{37}$$

where M is the number of nodes on the outlet boundary surface and $Flow_{in}$ is the mass fluxes through the inlet boundary surface.

6. Numerical results

In this section, the numerical results of the flow past a rotating and rotary oscillating circular cylinder for $Re = 200, 500$ and $1000, 0.5 \leq \alpha \leq 5.0$, and $0.1 \leq f_s \leq 2.0$ are presented and discussed. Table 1 shows the parameters for different computational cases in the investigation of the flow past a rotating circular cylinder, from which we can see in total 42 examples have been conducted. As the emphasis of this paper is to define the flow regime precisely, therefore, several cases in $2.0 \leq \alpha \leq 3.0$ have been chosen. We expect that the complete vortex suppression will occur in this range of α , and through the FFT analysis a certain critical value can be obtained to separate different flow regimes for each Re number. The center of the circular cylinder stands on the origin of the coordinate system, and the distances from the inlet boundary, outlet boundary, upper wall boundary and lower wall boundary to the origin are $10a, 30a, 10a$ and $10a$ respectively. 8840 triangular elements generated by the Delaunay triangulation method are adopted here, which are refined locally near the cylinder in order to ensure the accuracy of the numerical simulation. It should be mentioned that the mesh convergence test has been carried out for the flow past a fixed circular cylinder, and the convergent results have already been achieved at the meshes adopted here. The algebraic equation system is solved by the Gauss-Seidel method. The estimated convergence error of the inner iteration is the max relative error between two sequent iterations. The convergence criterion is 1×10^{-6} and the max iterative number is 50. The estimated convergence error of the outer iteration is the global mass flux residual, and the convergence criterion is 1×10^{-5} . The time step Δt is set to be 0.01 in all cases discussed below.

We can define the lift and drag coefficients by making use of the numerical solutions,

$$C_L = \frac{L}{\rho U_\infty^2 a}, \quad C_D = \frac{D}{\rho U_\infty^2 a} \tag{38}$$

where L and D are the lift and drag forces on the cylinder. It is known that the lift and drag coefficients consist of the components due to the friction force and the pressure,

$$C_L = \frac{2.0}{Re} \int_{S_b} \omega S_x dS + \int_{S_b} p S_y dS \tag{39}$$

$$C_D = -\frac{2.0}{Re} \int_{S_b} \omega S_y dS + \int_{S_b} p S_x dS \tag{40}$$

where ω is the viscous vorticity function, S_b denotes the cylinder surface and S_x and S_y are the area vector components in the Cartesian directions x and y respectively.

Table 1 Details of numerical examples for flow past a rotating circular cylinder

Re number	α	Number of cases
200	0.5, 1.0, 2.07, 2.1~ 3.1 (every 0.1), 3.25, 4.0	16
500	2.0 ~ 3.0 (every 0.1)	11
1000	0.5, 1.0, 2.0 ~ 3.0 (every 0.1), 4.0, 5.0	15

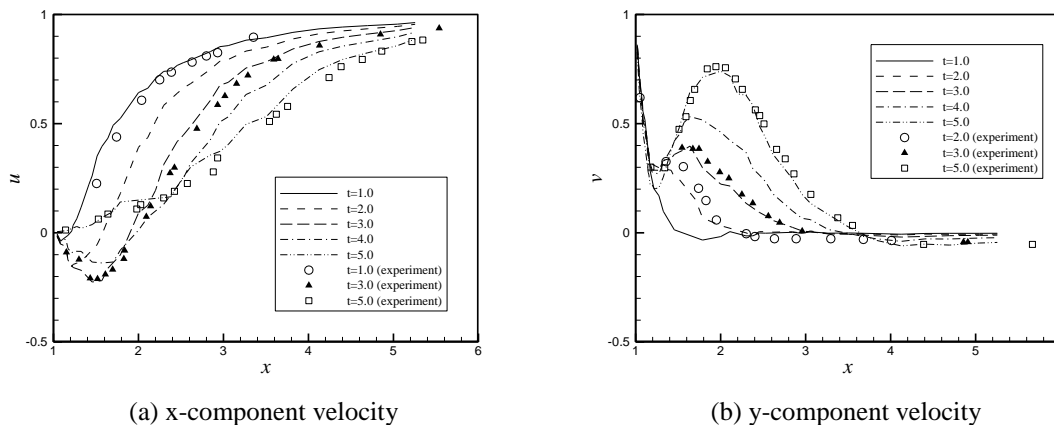


Fig. 4 Time development of velocity profile on the x -axis behind the circular cylinder and comparison with the experimental results of Coutanceau and Menard (1985) for $Re = 200$, $\alpha = 1$

6.1 Comparison of result for flow past a rotating cylinder at $Re = 200$

To demonstrate the validity of the present numerical results the initial velocity profiles are compared with the experimental results reported by Coutanceau and Menard (1985). Fig. 4 shows the temporal evolution of the velocity profile along the x -axis behind the circular cylinder for $\alpha = 1.0$ and $t \leq 5$. Good agreement with the experimental data has been achieved. The figure also indicates the growth of the attached vortex with respect to the time t , during which the u and v components approach to the free-stream value and zero respectively with increasing x . It should be noted that the lines in Fig. 4 are not very smooth. The reason is that the computational nodes may not locate exactly on the x -axis because of the asymmetrical distribution of the unstructured triangular elements adopted here. Therefore, a small distance to the x -axis may results in a small discrepancy to the desired smooth value.

As the ratio α increases, the vorticity layer generated at the upstream-moving side of the cylinder intensifies and as a consequence it becomes more difficult to maintain accuracy, as pointed out by Badr and Dennis (1985). However, the present numerical model is able to obtain the accurate numerical results by using the finer grids near the cylinder. Fig. 5 shows the instantaneous streamlines in the near wake for $\alpha = 2.07$ and $5 \leq t \leq 17$. Figs. 5(a) and 5(b) show that the first vortex grows gradually and moves in the downstream direction during the early stage of the flow. At the same time, the second vortex emerges at $t = 9.0$ in Fig. 5(b). It grows at $t = 13.0$

and 17.0 in Figs. 5(c) and 5(d). From the figure, it can be seen that the present numerical results validate the conclusion given by Coutanceau and Menard (1985) that no eddies appear in the lower wake for $\alpha = 2.07$. In addition, based on the comparison of the streamline pattern, the present numerical results calculated for the long dimensionless time are visually identical to that in Chen *et al.* (1993) for the same case.

6.2 Global characteristics of flow past a rotating cylinder

One of the central problems in Computational Fluid Dynamics is the accurate prediction of dynamic loads. The time histories of total lift and drag coefficients C_L and C_D for $Re = 200$ are shown in Fig. 6. Comparisons of the behavior of the lift and drag at small and large α show that when $\alpha = 2.07$, the lift and drag coefficients show regular fluctuations with a constant amplitude except during the initial stage of the flow. It is clear that the periodic fluctuation is related to the alternate vortex shedding. When $\alpha = 3.25$, the lift and drag coefficients become non-periodic. They tend to steady constant values after the steady state has been reached, which indicates that the vortex shedding may not be associated with the cylinder undergoing a high speed rotation. In addition, when $\alpha = 0$ corresponding to flow past a fixed cylinder we know that the drag coefficient fluctuates at twice the frequency of the lift coefficient, because the vortex in the wake is just oscillating across the symmetric centerline periodically. However, the lift and drag forces fluctuate at the same frequency when $\alpha \neq 0$ as shown in Fig. 6(a). When the cylinder is rotating, the vortex in the wake behind the cylinder is asymmetric and the different location of the vortex will result in a different drag force. Moreover, the difference in the amplitude of the drag coefficient is due to the location of the vortex in relation to the rear of the cylinder, which also causes the mean lift coefficient to move away from zero.

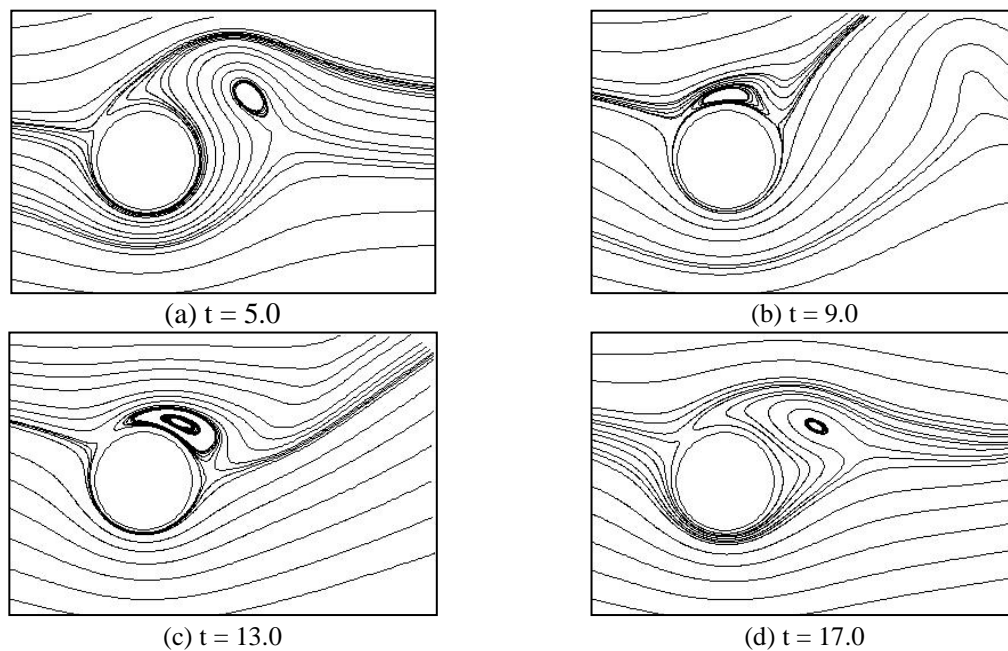


Fig. 5 Streamline pattern for $Re = 200$, $\alpha = 2.07$

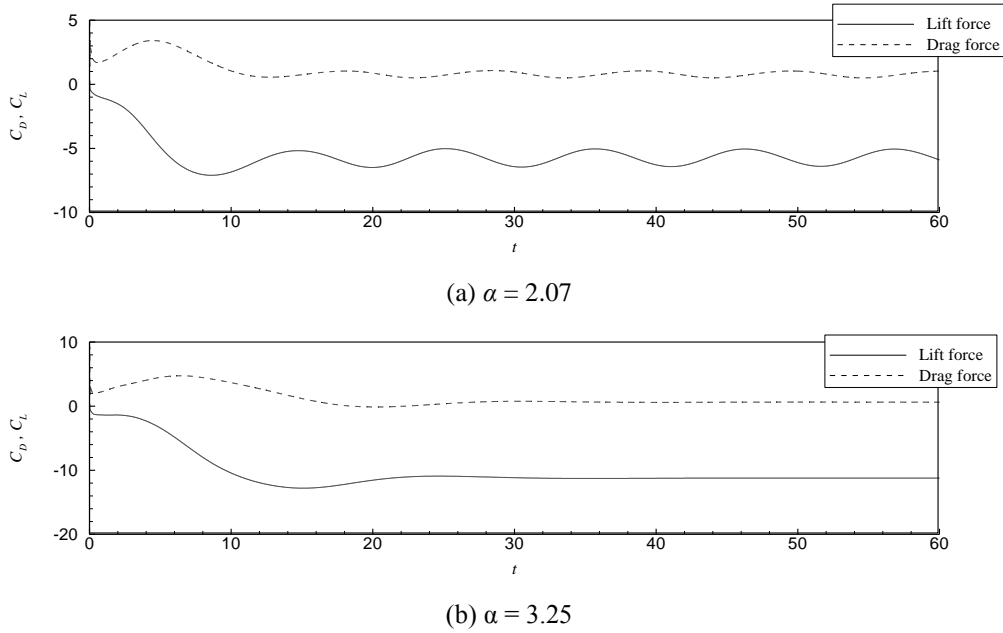


Fig. 6 Variation of the lift and drag coefficients with α and time for $Re = 200$

The shedding frequencies and the fluctuating amplitudes at various α for $Re = 200$ are obtained by the amplitude spectra analysis of the lift coefficients, as shown in Fig. 7. It is clearly seen that only one peak is observed in the amplitude spectrum with a particularly dominant frequency at all α . When $\alpha > 2.07$, the vortex shedding frequency decreases with the increase of α , and gradually moves away from the natural shedding frequency. At the same time, the fluctuating amplitude reduces rapidly and it is very small at $\alpha = 2.6$. This indicates that for $\alpha \geq 2.6$, any vortex shedding will disappear, the lift and drag forces become non-periodic and the flow structure turns to be steady.

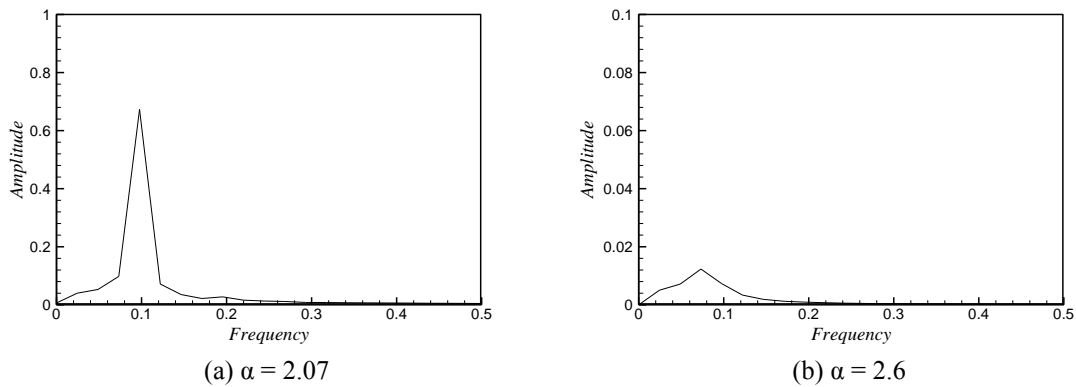


Fig. 7 Amplitude spectra of the lift coefficients at different α for $Re = 200$

The mean values of the lift and drag coefficients are shown in Fig. 8. The lift coefficients determined by the present method are similar to the results reported by Tokumaru and Dimotakis (1993) for $Re = 3800$, as both of them exceed the limiting magnitude of 4π . The existence of a limiting lift coefficient is proposed by Prandtl (1925) based on the theoretical analysis, and implies that the Magnus effect is only effective up to a certain α . However, in a real flow, the Görtler or Taylor vortices in the re-circulating region enclosed by the dividing closed streamline can alter the limiting lift coefficient phenomenon as observed in the present flow. It can be seen that the lift coefficient increases at a fast rate and the drag coefficient varies in a small range with the increase of α . When $\alpha \leq 2 \sim 3$, the higher the α , the smaller is the drag coefficient because the location of the vortex behind the cylinder moves to the top of the cylinder, and the flow field changes to be symmetric between the upstream and downstream of the cylinder gradually. With the disappearance of Kármán vortex street, the drag coefficient increases and tends to approach an asymptotic value.

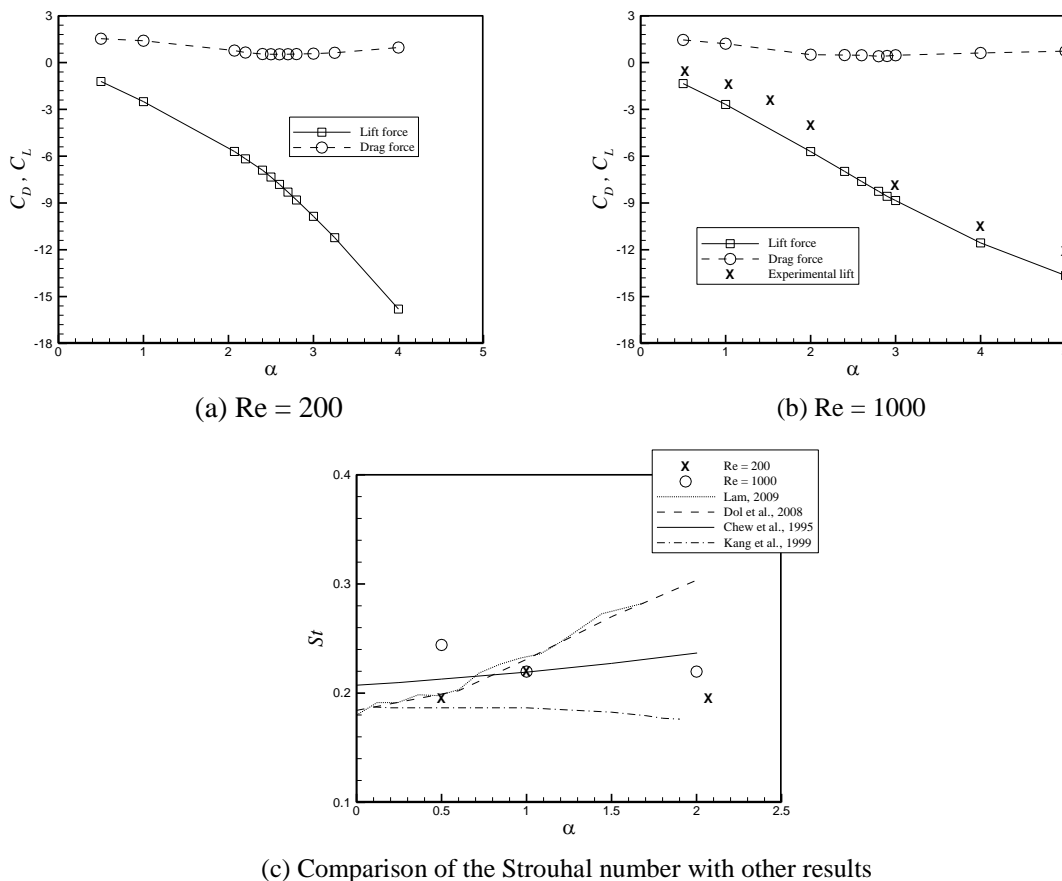


Fig. 8 Variation of the mean lift and drag coefficients, and the Strouhal number with α

For the purpose of comparison, the lift coefficients reported by Tokumaru and Dimotakis (1993) for $Re = 3800$ are also included in Fig. 8(b). We can notice that our lift coefficients are over-predicted. However, it should be noted that we are comparing the results at different Re numbers (the present results are given for $Re = 1000$). Nevertheless, they follow the same trend and a higher Re number will generally lead to a smaller lift force. This conclusion can be also drawn from the comparison of the lift coefficients at $Re = 200$ and $Re = 1000$. The comparison is also made for the Strouhal number when $\alpha \leq 2$ with the results report by Dol *et al.* (2008) for $Re = 9000$, Lam (2009) for $Re = 5000$, Chew *et al.* (1995) for $Re = 1000$ and Kang *et al.* (1999) for $Re = 160$, as shown in Fig. 8(c). The Strouhal number is determined by means of the FFT analysis which is known to be sensitive to the sample chosen. Time interval, sample duration and beginning point are the factors influencing the FFT results. However, it can be seen that the present Strouhal numbers fall into the range of others' results. From the comparisons of the lift coefficient and Strouhal number, the present numerical model is well validated.

The amplitude spectra analysis of the lift coefficients shows that when the fluctuating amplitude is small enough to be ignored, the Kármán vortex street vanishes. It is necessary to notify that this critical value of α is the same with that at which the minimum drag coefficient is obtained. Using the critical value of α for variant Reynolds numbers, we give the regions of the classification of vortex shedding patterns behind the cylinder in Fig. 9. In the figure, only three points are available at three different Re numbers. However, a fitting curved line is also drawn in the figure to clearly indicate the separation of different regions. Region R_1 represents the wake of the cylinder is steady and no vortices are shed, and Region R_2 denotes the alternating vortices are shed from the upper and lower sides of the cylinder. This figure can provide important references for the reduction of flow-induced vibrations in ocean engineering.

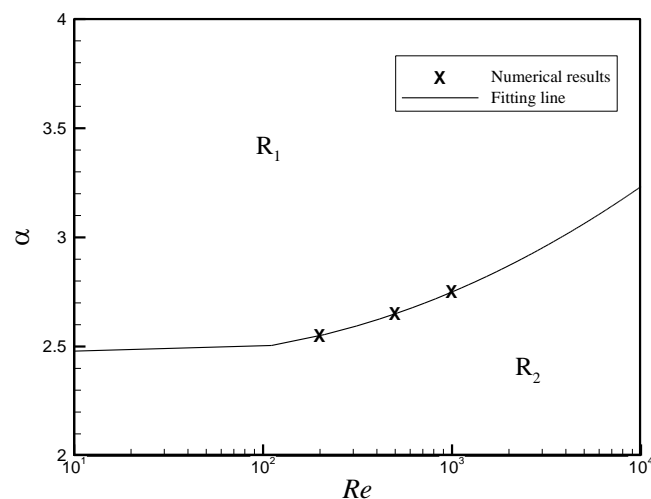


Fig. 9 The regions of the classification of vortex shedding pattern behind the rotating cylinder

6.3 Global characteristics of flow past an oscillating cylinder

In this section, 92 cases are chosen to investigate the flow past a rotary oscillating circular cylinder, and the detailed information for those cases can be found in Table 2. Before the dynamic loads on a rotary oscillating cylinder are discussed, we will now show how the flow evolves when Re and α remain fixed at 200 and 2 respectively. Fig. 10 gives the patterns of instantaneous streamlines for $f_s = 0.2$ over one period of vortex shedding, which have turned to be periodic after $t = 20$. It can be seen clearly that the vortex shedding and the forced oscillation of the cylinder finish the variation over one period at the same time. The flow evolution is similar to that in the early stage of the wake development. An eddy emerges on the upper or lower side of the cylinder per half-cycle. Then, it separates from the cylinder and moves in the downstream direction. Lastly, the eddy decreases, splits and vanishes gradually with increasing time. The evolution indicates the vortex shedding is synchronized by the cylinder oscillation.

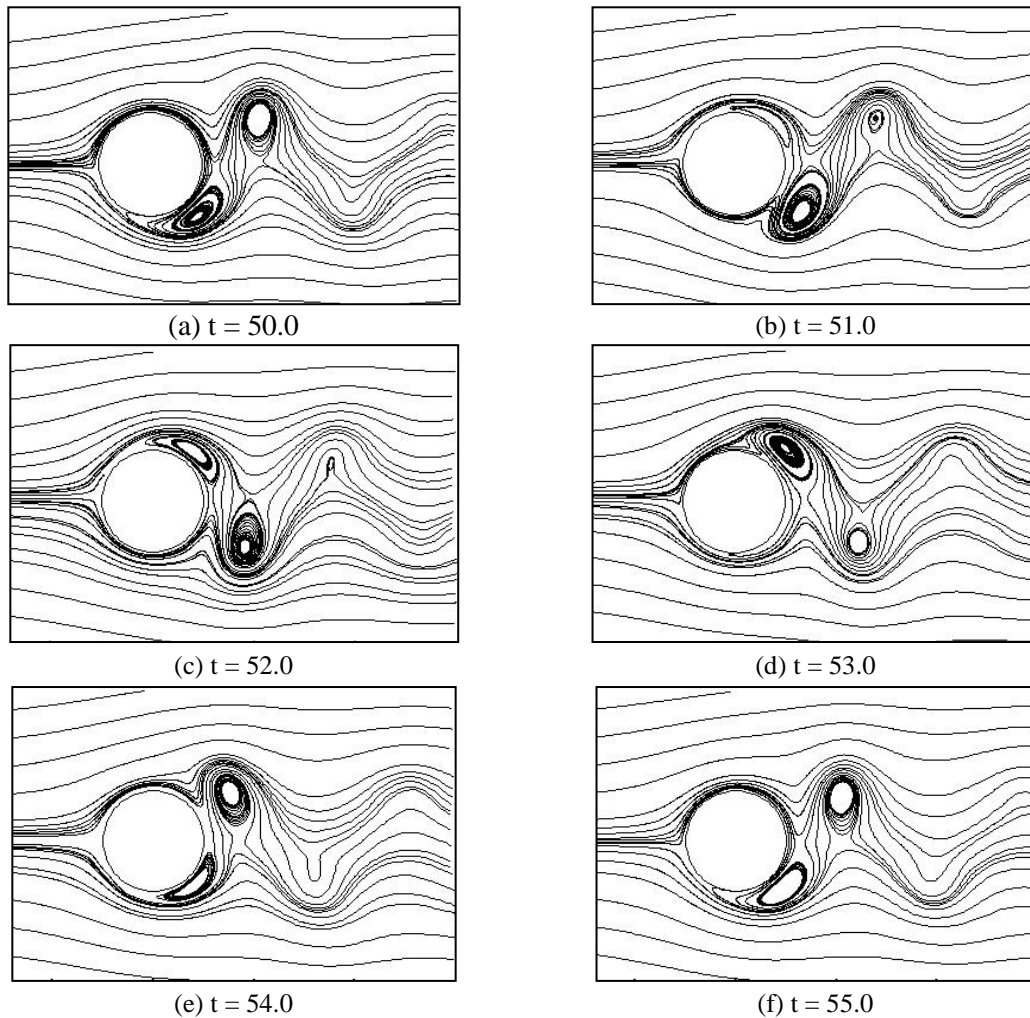
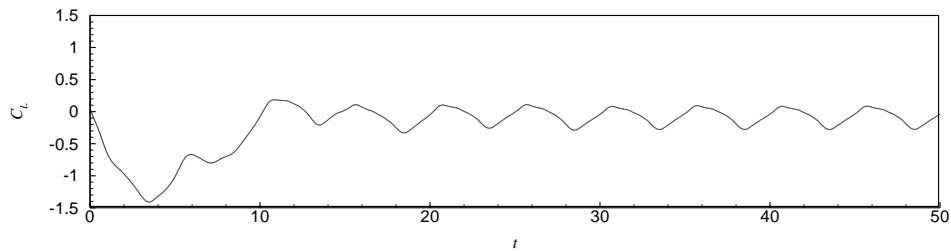
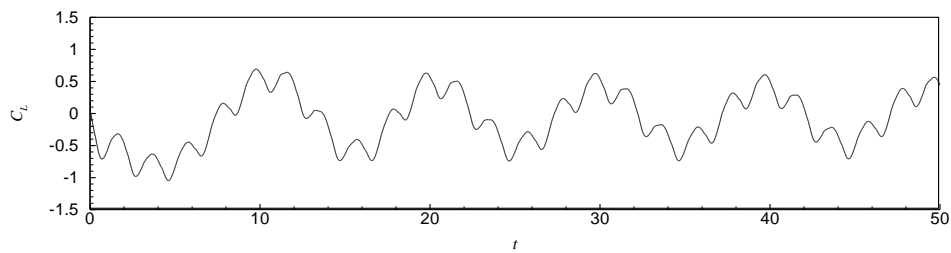
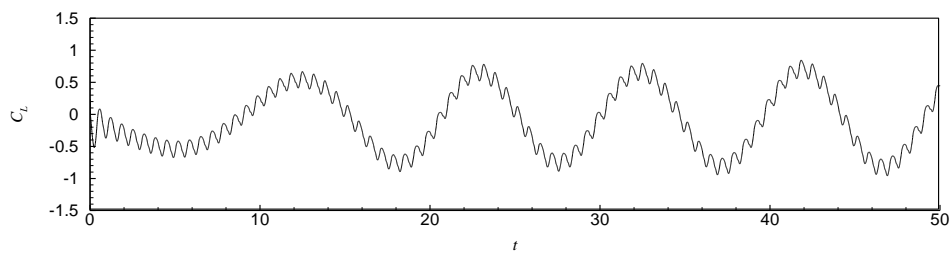


Fig. 10 Patterns of instantaneous streamlines for $Re = 200$, $\alpha = 2$, $f_s = 0.2$

Table 2 Details of numerical examples for flow past a rotary oscillating circular cylinder

Re number	α	f_s	Number of cases
200	0.5	0.1~2.0 (every 0.1)	20
	2.0	0.1~2.0 (every 0.1)	20
	4.0	0.1~2.0 (every 0.1)	20
1000	0.5	0.1~1.0 (every 0.1)	10
	2.0	0.1~1.0 (every 0.1), 1.5	11
	4.0	0.1~1.0 (every 0.1), 1.5	11

(a) $f_s = 0.2$ (b) $f_s = 0.5$ (c) $f_s = 1.5$ Fig. 11 Variation of the lift coefficients with f_s and time for $Re = 200$, $\alpha = 2$

The time histories of the lift coefficient C_L for $Re = 200$ and $\alpha = 2$ are shown in Fig. 11. It is clear that the lift coefficient shows periodic variation related to the alternate vortex shedding except during the starting stage of the flow. When $f_s = 0.2$, the lift coefficient fluctuates with a

constant amplitude like a sinusoid at the forced oscillating frequency owing to the results of the ‘synchronization’ effect. With increasing f_s , the lift coefficients tend to oscillate at the natural shedding frequency as a whole, but some fluctuations at the forced oscillating frequency appear. The amplitude at the higher frequency is comparable with that at the lower frequency $f_s = 0.5$, and it becomes much smaller for $f_s = 1.5$ indicating the natural shedding frequency occupies an important place.

Fig. 12 is the variation of the drag coefficients with f_s for $Re = 200$ and $\alpha = 2$. At $f_s = 0.2$, the drag and lift forces fluctuate at the same frequency, but we can observe some nonlinear influences at higher harmonics. As shown in Fig. 12(b), the drag coefficient becomes irregular, fluctuating at neither the forced frequency nor the natural frequency. This case is the best example to illustrate the competitive relationship between the frequencies. When $f_s = 1.5$, the drag coefficient fluctuates at twice the frequency of the lift coefficient, which is similar to the case of flow past a stationary cylinder. Furthermore, the amplitude at the higher frequency is almost equal to that at the lower frequency, which shows that the cylinder oscillation has more effect on the drag coefficient.

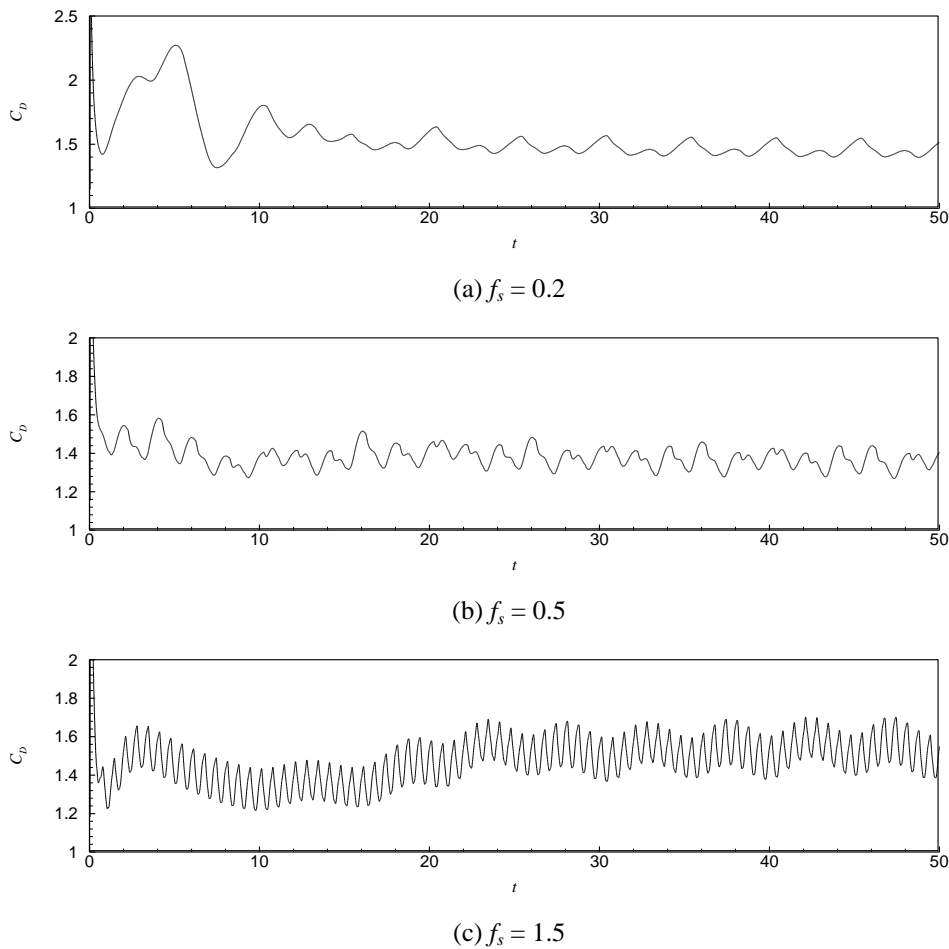


Fig. 12 Variation of the drag coefficients with f_s and time for $Re = 200$, $\alpha = 2$

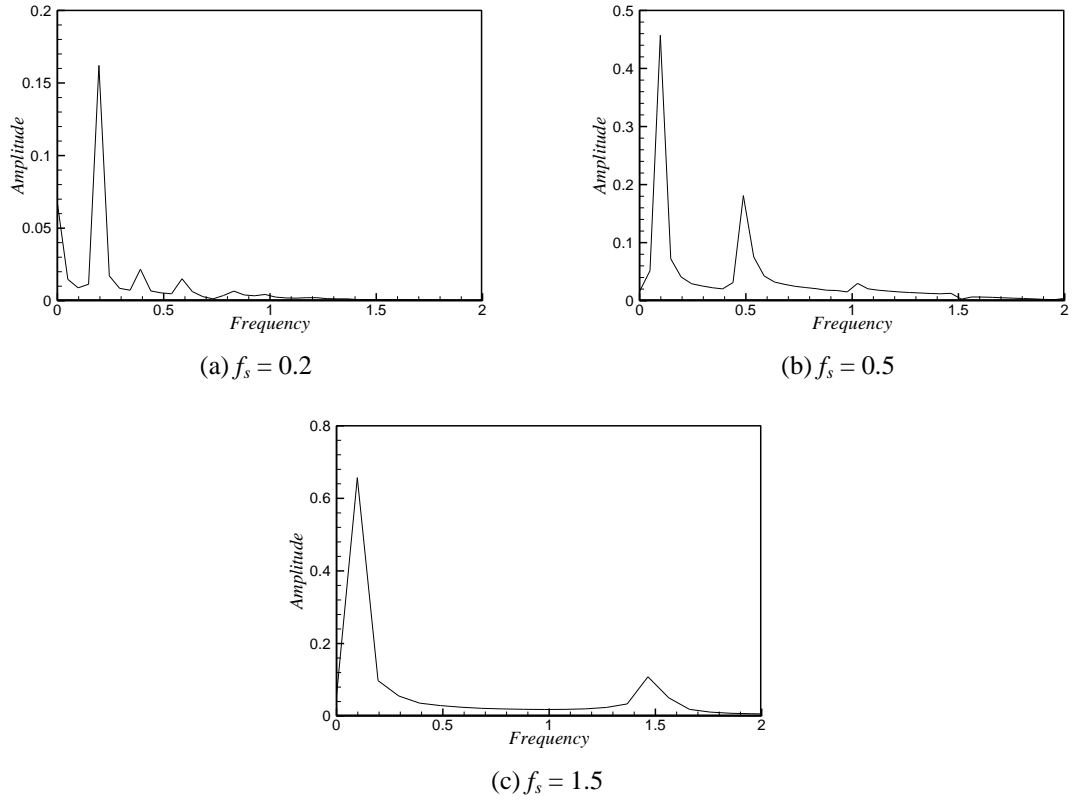


Fig. 13 Amplitude spectra of the lift coefficients at different f_s for $Re = 200$, $\alpha = 2$

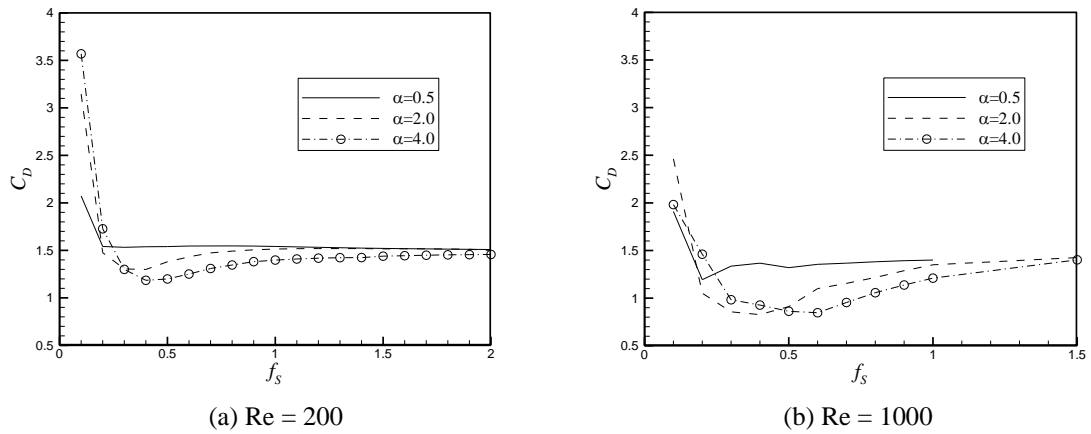


Fig. 14 Variation of the mean drag coefficients with α and f_s

The shedding frequencies and the fluctuating amplitudes at various f_s for $Re = 200$, $\alpha = 2$ are obtained by using the amplitude spectra of the lift coefficient as shown in Fig. 13. When $f_s = 0.2$,

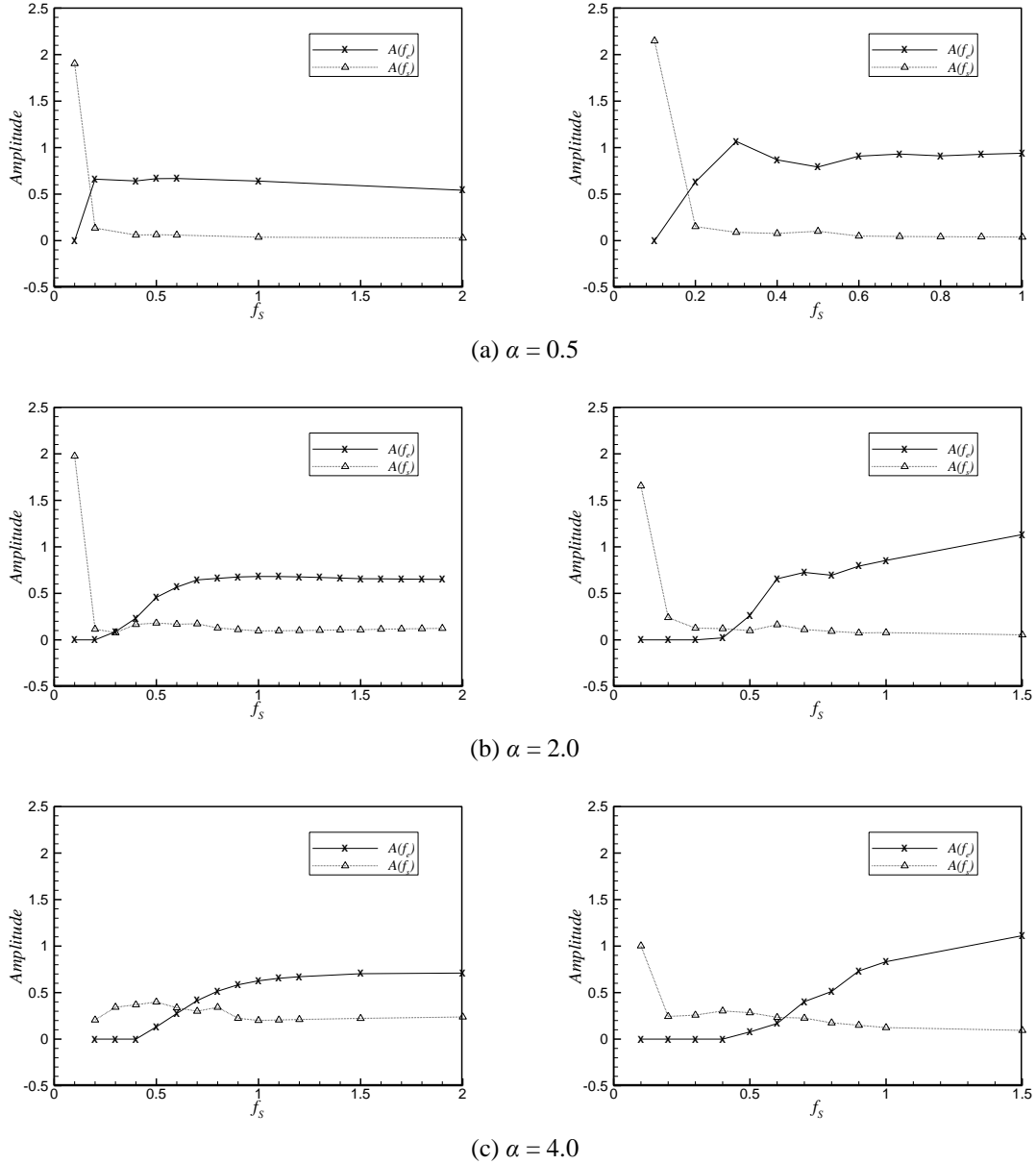
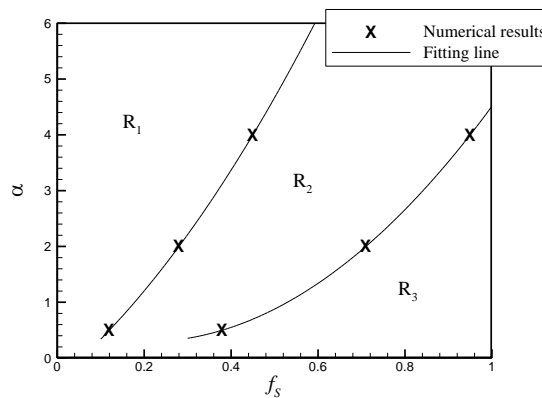


Fig. 15 Variation of the amplitudes of the lift coefficients corresponding to natural shedding frequency $A(f_e)$ and oscillating frequency $A(f_s)$ with α and f_s for $Re = 200$ (left) and $Re = 1000$ (right)

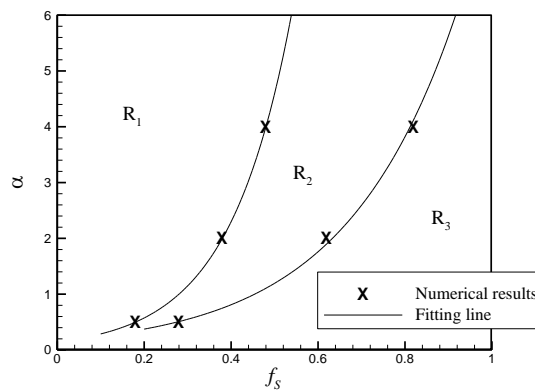
only one leading peak is observed in the amplitude spectrum, and the particularly dominant frequency corresponds to the forced oscillating frequency. We also find the nonlinear feature of the flow due to the appearance of some minor peaks in Figs. 13(a) and 13(b). Above $f_s \approx 0.2$, the flow structure depends on two frequencies: one is the forced oscillating frequency and the other is the

natural shedding frequency. From the comparison of amplitudes in Figs. 13(b) and 13(c), we observe that the fluctuating amplitude at the forced oscillating frequency reduces, while the natural shedding frequency increases with the increase of f_s .

The mean values of the drag coefficients are shown in Fig. 14. The present results are qualitatively similar to the figure given by Tokumaru and Dimotakis (1991) for $Re = 1.5 \times 10^4$ who reported that when f_s is less than a certain value, the drag coefficient initially decreases with increasing f_s and then it increases. When the oscillating frequency is equal to the natural shedding frequency at 0.1, the maximum drag coefficient is obtained due to the effect of resonance. The drag coefficient reduces rapidly in the ‘synchronization’ region. It comes to the minimum value when the flow structures begin to show the ‘competition’ mode for $Re = 200$. However for $Re = 1000$, it seems that the appearance of the minimum value is deferred a little from the starting point of the ‘competition’ mode. With the appearance of Kármán vortex street, the drag coefficient increases and tends to approach an asymptotic value which agrees with the force of flow past a fixed cylinder. The relatively smaller drag coefficients obtained in the ‘competition’ region indicate the cylinder oscillation is an efficient measure to reduce the flow-induced force.



(a) $Re = 200$



(b) $Re = 1000$

Fig. 16 The regions of the classification of vortex shedding pattern behind the rotary oscillating cylinder

Fig. 15 is the fluctuating amplitudes at different frequencies determined by the amplitude spectra analysis of the lift coefficients, where $A(f_e)$ is the amplitude at the natural shedding frequency, and $A(f_s)$ denotes the amplitude at the forced oscillating frequency. It illustrates clearly the frequency-coupling feature of the flow, and the criterion for classifying the flow modes into three types. When $A(f_e) = 0$, because only the oscillating frequency exists and controls the vortex shedding in the wake, we define the flow as in the 'synchronization' mode. As $A(f_e)$ becomes larger from zero and $A(f_s)$ decreases from the maximum value, the two frequencies influence the flow structure together and we thus define the flow as in the 'competition' mode. When $A(f_e)$ and $A(f_s)$ tend to approach an asymptotic value at the same time, moreover $A(f_s)$ is much smaller compared with $A(f_e)$, we define the flow as the 'natural shedding' mode. It also can be seen that the fluctuating amplitudes are reduced by the cylinder oscillation.

Using the classification criterion discussed above, we give the regions of the classification of vortex shedding pattern behind the cylinder in Fig. 16. Regions R_1 , R_2 , and R_3 represent the 'synchronization', 'competition', and 'natural shedding' modes respectively. For larger Re , the 'competition' region becomes narrower, and the 'natural shedding' mode occurs earlier. This figure is proposed to be the guidance for new studies and realistic engineering problems.

7. Conclusions

In this paper, a FVM based on the unstructured triangular collocated grids is adopted to investigate the flow development around a rotating and rotary oscillating circular cylinder at $Re = 200$ and 1000 by solving numerically the Navier-Stokes equations. For the flow past a rotating cylinder, the present numerical computation confirms the flow features in the near wake at the initial stage observed in the experiments and other numerical studies. A critical value of α is determined by the amplitude spectra analysis of the lift coefficient, above which the vortex shedding ceases. The paper presents the regions of the classification of vortex shedding pattern behind the cylinder, predicting the domain in which the steady wake can be achieved. For the flow past a rotary oscillating cylinder, the mean drag coefficient decreases with increasing f_s up to a critical value which almost corresponds to the starting point of the 'competition' mode, and then increases and tends to approach an asymptotic value. The results indicate that the cylinder oscillation is an efficient measure to reduce the flow-induced force and flow-induced vibration. After determining the fluctuating amplitudes at different frequencies by the amplitude spectra analysis of the lift coefficients, the regions of the classification of vortex shedding pattern behind the cylinder are presented, which is an important reference for the similar problems in ocean engineering.

References

- Badr, H.M., Coutanceau, M., Dennis, S.C.R. and Menard C. (1990), "Unsteady flow past a rotating circular cylinder at Reynolds numbers 10^3 and 10^4 ", *J. Fluid Mech.*, **220**, 459-484.
- Badr, H.M. and Dennis, S.C.R. (1985), "Time-dependent viscous flow past an impulsively started rotating and translating circular cylinder", *J. Fluid Mech.*, **158**, 447-488.
- Baek, S.J. and Sung, H.J. (1998), "Numerical simulation of the flow behind a rotary oscillating circular cylinder", *Phys. Fluids*, **10**(4), 869-876.
- Bishop, R.E.D. and Hassan, A.Y. (1964), "The lift and drag on a circular cylinder oscillating in a flow field",

- Proc. R. Soc. Lond. A*, **277**, 51-75.
- Chen, Y.M., Ou, Y.R. and Pearlstein, A.J. (1993), "Development of the wake behind a circular cylinder impulsively started into rotatory and rectilinear motion", *J. Fluid Mech.*, **253**, 449-484.
- Cheng, C.C. and Chern, R.L. (1991), "Vortex shedding from an impulsively started rotating and translating circular cylinder", *J. Fluid Mech.*, **233**, 265-298.
- Chew, Y.T., Cheng, M. and Luo, S.C. (1995), "A numerical study of flow past a rotating circular cylinder using a hybrid vortex scheme", *J. Fluid Mech.*, **299**, 35-71.
- Dol, S.S., Kopp, G.A. and Martinuzzi, R.J. (2008), "The suppression of periodic vortex shedding from a rotating circular cylinder", *J. Wind Eng. Ind. Aero*, **96**(6-7), 1164-1184.
- Coutanceau, M. and Menard, C. (1985), "Influence of rotation on the near-wake development behind an impulsively started circular cylinder", *J. Fluid Mech.*, **158**, 399-446.
- Diaz, F., Gavalda, J., Kawall, J.G., Keffer, J.F. and Giral, F. (1983), "Vortex shedding from a spinning cylinder", *Phys. Fluids*, **26**(12), 3454-3460.
- Ferziger, J.H. and Perić, M. (1999), *Computational methods for fluid dynamics*, Springer, Berlin Heidelberg.
- Kang, S., Choi, H. and Lee, S. (1999), "Laminar flow past a rotating circular cylinder", *Phys. Fluids*, **11**(11), 3312-3321.
- Karabelas, S.J. (2010), "Large eddy simulation of high-Reynolds number flow past a rotating cylinder", *Int. J. Heat Fluid Flow*, **31**(4), 518-527.
- Koopman, G.H. (1967), "The vortex wakes of vibrating cylinders at low Reynolds numbers", *J. Fluid Mech.*, **28**(3), 501-512.
- Koromilas, C.A. and Telionis, D.P. (1980), "Unsteady laminar separation: an experimental study", *J. Fluid Mech.*, **97**(2), 347-384.
- Lam, K.M. (2009), "Vortex shedding flow behind a slowly rotating circular cylinder", *J. Fluids Struct.*, **25**(2), 245-262.
- Li, P.W. and Tao, W.Q. (1993), "Numerical and experimental investigations on heat/mass transfer of slot-jet impingement in a rectangular cavity", *Int. J. Heat Fluid Flow*, **14**(3), 246-253.
- Lu, X.Y. and Zhuang, L.X. (1994), "Numerical study of viscous flow past a rotating circular cylinder in a uniform stream", *ACTA Mech. Sinica*, **26**(2), 233-238 (in Chinese).
- Matsui, T. (1982), *Flow visualisation studies of vortices*, (Ed. Narasimha, R. and Deshpande, S.M.), Survey in Fluid Mechanics, Macmillan.
- Mittal, S. (2001), "Control of flow past bluff bodies using rotating control cylinders", *J. Fluids Struct.*, **15**(2), 291-326.
- Nobari, M.R.H. and Ghazanfarian, J. (2009), "A numerical investigation of fluid flow over a rotating cylinder with cross flow oscillation", *Comput. Fluids*, **38**(10), 2026-2036.
- Okajima, A., Takata, H. and Asanuma, T. (1975), *Viscous flow around a rotational oscillating circular cylinder*, Report, Inst. Space & Aero. Sci., University of Tokyo.
- Prandtl, L. (1925), "The Magnus effect and windpowered ships", *Naturwissenschaften*, **13**, 93-108.
- Rao, A., Stewart, B.E., Thompson, M.C., Leweke, T. and Hourigan, K., (2011), "Flows past rotating cylinders next to a wall", *J. Fluids Struct.*, **27**(5-6), 668-679.
- Swanson, W.M. (1961), "The Magnus effect: a summary of investigation to date", *J. Basic Eng.*, **83**(3), 461-470.
- Taneda, S. (1980), *Visualization of unsteady flow separation*. (Ed. Merzkirch, W.), Flow Visualization II, Hemisphere.
- Tokumaru, P.T. and Dimotakis, P.E. (1991), "Rotary oscillation control of a cylinder wake", *J. Fluid Mech.*, **224**, 77-90.
- Tokumaru, P.T. and Dimotakis, P.E. (1993), "The lift of a cylinder executing rotary motions in a uniform flow", *J. Fluid Mech.*, **255**, 1-10.
- Yoon, H.S., Chun, H.H., Kim, J.H. and Park, I.L.R. (2009), "Flow characteristics of two rotating side-by-side circular cylinders", *Comput. Fluids*, **38**(2), 466-474.